International Journal of Heat and Mass Transfer 270 (2026) 129157

Contents lists available at ScienceDirect

International Journal of Heat and Mass Transfer

journal homepage: www.elsevier.com/locate/hmt

Parametric estimation of heat transfer coefficient: Incorporating boundary losses for enhanced accuracy

Sandeep R. Kumar [a], Kalyana B. Nakshatrala [b,*], Jason F. Patrick [c,*]

[a] Department of Mechanical and Aerospace Engineering, North Carolina State University, 27695, Raleigh, USA
[b] Department of Civil Engineering, University of Houston, 77204, Houston, USA
[c] Department of Civil, Construction, and Environmental Engineering, North Carolina State University, 27695, Raleigh, USA

ARTICLE INFO

Keywords:
Heat transfer coefficient
Boundary losses
Parametric estimation
Reduced-order modeling

ABSTRACT

Thermal regulation of structural components is critical to modern applications, particularly those subjected to erratic operating conditions and environments. For instance, space probe solar panels and electric vehicle battery packaging avail vascular-based active cooling via fluid circulation to safeguard these critical onboard assemblies from thermal overload during charging/discharging. To conduct systematic heat transfer studies—involving modeling and/or experimentation—and develop suitable designs, it is essential to estimate the convective heat transfer coefficient (HTC). While the convective HTC, herein denoted by h_{conv}, is a useful parameter, it is neither a material property nor a fundamental thermodynamic quantity, and is thus challenging to accurately estimate. Precise measurement of h_{conv} from thermal experiments requires either achieving adiabatic conditions (a theoretical ideal often not realized in practice) or quantifying boundary loss (a random and nonlinear phenomenon). Additionally, thermal measurements, such as those obtained with infrared (IR) imaging, are prone to noise, further complicating the calculation. To overcome these challenges, we propose a new approach that combines experimental transient thermal measurements (together with noise filtering techniques) and a parametric estimation method based on a reduced order model (ROM). This approach allows one to determine both the convective HTC and boundary loss simultaneously and systematically. Moreover, incorporating boundary loss into the calculation of h_{conv} enhances the accuracy, which in turn leads to higher fidelity numerical models that can be used to better understand and design more efficient thermal regulation systems.

1. Opening remarks

Heat flow between a body and its surroundings can be regulated by the appropriate choice of a medium (or the absence of such) at the interface/boundary between them. For instance, if the interface is a vacuum, then unlike heat transfer via radiation, conduction and convection—both of which require a physical medium—can be evaded. Most applications, however, cannot accommodate a vacuum seal due to operational constraints, and must therefore rely on materials that minimize heat flow through the interface. This is typically accomplished using materials of low thermal conductivity (i.e., insulators). However, every material has a finite value of thermal conductivity, no matter how small. Therefore, undesirable heat flow cannot be fully arrested, but rather minimized to varying degrees of effectiveness depending on the properties of the insulator, and the contact between the insulator and object of interest. Consequently, the ideal “adiabatic” boundary becomes impractical to achieve in a physical application and is often realized as *nearly* adiabatic, with a finite heat leakage (i.e., boundary loss) occurring through it.

On the other hand, analytical and numerical models for thermal systems often employ the simpler alternative of adiabaticity to represent such boundaries [1,2]. Parity between models (that assume adiabaticity) with experiments that contain realistic boundaries (with losses) is only possible if the heat loss through the boundaries can be accurately quantified. In the absence of an estimate for boundary heat loss, thermal models are prone to predicting larger design heat loads, calling for higher capacity cooling systems than might be actually required. Though conservative, over-design can be a severe challenge to overcome especially in applications where component size, weight, power, and cost (SWaP-C) are critical, necessitating accurate estimates of every mode of thermal interaction including heat loss through the boundary [3,4].

Quantification of boundary loss has additional utility in the estimation of the convective heat transfer coefficient. Unlike thermal

* Corresponding authors.
E-mail addresses: knakshatrala@uh.edu (K.B. Nakshatrala), jfpatric@ncsu.edu (J.F. Patrick).

https://doi.org/10.1016/j.ijheatmasstransfer.2026.129157
Received 1 March 2026; Received in revised form 5 June 2026; Accepted 9 June 2026
Available online 20 June 2026
0017-9310/

conductivity which is a material property, h_{conv} is a parameter that encapsulates the effect of various underlying solid-fluid interactions that develop in the thermal and hydrodynamic boundary layers. Estimation of h_{conv} relies on empirical relations based on the shape of the solid, its orientation with respect to the direction of fluid flow, and the nature of the fluid flow [5–8]. However, flow conditions can vary over the geometry of the solid leading to locally varying convective HTC values. Empirical relations can provide average values of h_{conv}, but generally do not encompass spatially varying convective fields [9–11].

An alternate approach to estimate h_{conv} is to use Newton's law of cooling [12–14]. This approach relies on the balance of thermal energy between the heat input to the system and the heat lost through convection, advection, radiation, and conduction. The energy balance equation can only be used to discern one unknown quantity. If the heat transferred by convection (i.e., h_{conv}) is known, boundary heat loss can be estimated (provided all the other components of heat transfer are known). Alternatively, if the boundary heat loss is known, the convective heat transfer—and consequently h_{conv}—can be determined. This gives rise to a conundrum where the knowledge of one is required for the estimation of the other, i.e., neither quantity can be determined without knowing the other.

In order to circumvent this challenge, studies that focus on convective heat transfer often utilize geometries that minimize the area through which conductive losses could potentially occur [15,16]. For instance, a cylinder suspended in a stream of fluid experiences convective heat transfer over its entire curved surface as well as its end faces, with minimal conductive losses occurring through material contact via the suspension mechanism [17,18]. Furthermore, when studied within enclosed domains, the convecting surfaces are kept sufficiently far away from the boundaries of the enclosure, further minimizing the contribution of conductive boundary losses [19].

On the other hand, boundary heat loss has been studied extensively where convection is not as significant—such as thermal losses in underground pipes, building insulation, etc. [20–22]. Studies on the efficient design of combustion chambers aiming to quantify and minimize conductive heat loss (heat leakage) often bundle heat interactions occurring at the exterior walls into a heat load/sink which, being design inputs, are known *a priori* [23,24]. However, there are several geometries where both convective heat transfer as well as comparable conductive heat losses occur, and need to be accounted for (i.e., estimated) simultaneously.

An example of this scenario occurs in experimental studies of actively-cooled flat, rectangular plates [25–28]. Heat is supplied to the plate through its bottom surface by means of an external heater, and the plate is actively cooled by circulating fluid through it. The plate-heater assembly is placed on an insulating platform, and all four lateral surfaces of the assembly are insulated. The top surface of the material, however, is free to convect and radiate. Several studies involving such test configurations consider conductive heat loss occurring through the insulating platform and lateral boundaries to be zero, i.e., perfectly insulated [28–31]. By extension, corresponding numerical models also assume adiabatic conditions on the respective boundaries [32–34]. However, evidence of this assumption being a departure from the actual test conditions has also been observed in prior work, where predictions from simulations that consider adiabatic boundaries vary from experimental results [35–37]. With (i) undesirable conductive heat loss occurring through four lateral surfaces and the bottom surface resting on the insulating platform, and (ii) convective (and radiative) heat transfer occurring through the entire top surface of the plate, the thermal test configuration provides for non-negligible contributions from both convective and conductive heat losses.

Radiation is another heat transfer phenomenon, but estimating this contribution involves conveniently measurable quantities—the Stefan–Boltzmann constant (a known value), ambient and surface temperatures, and emissivity, which is a surface property with a well-defined measurement procedure [38]. While radiation inherits nonlinearity with respect to the temperature field that is difficult to handle analytically, heat transferred via this mode can be accurately estimated through experimental measurements [39–42]. Thus, the challenge for determining reliable heat transfer properties largely remains in the treatment of the convective HTC and conductive boundary loss. Analytical methods to determine these quantities require mathematical simplification of the remaining nonlinear radiation term. This is commonly accomplished by lumping the radiative with the convective component to determine a combined heat transfer coefficient (h_{comb}) during analytical inquiry, and subsequently deducting the measured radiative component to back calculate the convective HTC (h_{conv}).

In keeping with that process, the present work provides an innovative parametric estimation technique to simultaneously estimate both, h_{comb} as well as boundary loss using experimentally obtained temperature evolution data. Parametric estimation is a powerful tool employed to study inverse problems [43–45]. The technique has been applied to thermal problems, often to estimate more than one unknown parameter, as is the case for our study here [46–50]. Using the typical active-cooling experimental setup previously described for demonstration of the technique, we present a novel procedure (including an experimental protocol and a modeling approach accounting for noise) to accurately estimate the combined heat transfer coefficient, including the effects of boundary losses through optical-based thermal measurements. This new approach successfully combines reduced-order modeling, parametric estimation, infrared (IR) imaging, and noise filtering algorithms to overcome a longstanding challenge.

The article is organized as follows. Section 2 provides further motivation to carry out this work. Section 3 details the analytical model which forms the basis to extract the quantities of interest, along with the details of the data filtering technique. Section 4 provides the details of the experimental methodology followed to extract the thermal response of the materials being studied, while Section 5 presents the findings of the study. We end the paper with concluding remarks in Section 6.

2. Motivation and approach

A discussion around the challenges with the active-cooling setup that is selected to demonstrate our estimation technique best highlights the motivation behind our approach and its novelty.

Active cooling is a thermal regulation mechanism in which a fluid (coolant) is circulated through a material while it remains in service under a thermal load [51–55]. Active-cooling experiments, therefore, need to incorporate three elements: (1) a heat source, (2) an active-cooling network consisting of internal flow channels connected to (3) a circulating pump. A common heat source used in active-cooling experiments is resistive heaters, which can either be embedded within the specimen if the material allows for such a construction (e.g. laminated composites), or used as an external element in the form of a heating coil [2,56]. In either case, the resistive heaters produce a non-uniform heat flux. In case of embedded heaters, the inherent non-uniform distribution of electrical current through conductive constituents and electrical connections give rise to heat flux non-uniformity. In the case of external heaters, heat flux non-uniformity arises due to the imperfect contact interface and discrete geometry of the heating coil as seen in the measured IR temperature contour shown in Fig. 1a. Controlled active-cooling studies, however, require a constant and uniform heat flux input for parity with analytical and computational models [57–59]. While the non-uniformity arising from embedded heaters is difficult to correct, that from external heaters can be mitigated by using an intermediate plate of high thermal conductivity (such as copper) placed between the heater coil and the actively-cooled body (Fig. 1b). In the parlance of the experimental setup, we refer to this component as the "base plate". Such discourse raises the following questions:

(Q1) What are the ramifications in selection of the base plate material and geometry (prescribed to produce a reasonably uniform thermal load) on the heat transfer coefficient and boundary heat loss?

Due to its superior conductivity and finite thickness, the base plate enhances heat flux uniformity, but also increases the propensity for heat loss through the boundaries. Hence, the lateral sides of the base plate are insulated (Fig. 1c). Moreover, the base plate/heater assembly is placed on an insulating platform to minimize heat loss from the bottom face. Consequently, we ponder:

(Q2) What are the material and geometrical specifications of the insulation?

The insulation material has a finite (albeit small) thermal conductivity, allowing for heat loss by conduction through its bulk. IR thermography of the top face of the base plate surrounded on all four sides by lateral insulation (Fig. 1c) shows a temperature gradient across the width of the lateral insulation, providing evidence of conductive heat loss. On all four sides, the temperature of the insulation goes from that of the base plate (white-dashed box) to the ambient temperature at its outer edges. As is the case with lateral insulation, the bottom insulating platform too has a finite conductivity, and therefore leads to through-thickness heat loss as well. Thus, we pose:

(Q3) Given that perfect adiabatic conditions are not attainable in practice, how can boundary losses be accounted for to accurately calculate the heat transfer coefficient (HTC)?

During thermal experiments, an IR camera mounted overhead is used to track the surface temperature of the assembly as shown in Fig. 2a. The IR camera captures point-wise temperature every few seconds across the actively-cooled material as well as the lateral insulation. The readings are subject to influences from continuously changing ambient temperature and air-flow conditions, as well as internal deviations due to drift within the electronic components of the camera. These factors produce small fluctuations in the recorded temperature, i.e., "noise". As shown in Fig. 2b, the time scale of the associated thermal noise is on the order of seconds, while the temperature evolution is on the order of several minutes. Consequently, noise adds a spurious variation in the data that does not reflect realistic temperature changes, and negatively impacts accurate estimation of the HTC. Therefore, we seek to understand:

(Q4) How can the noise in infrared thermal measurements be filtered out to improve the accuracy of the HTC calculations?

Our innovative approach to construct a framework for accurately calculating the HTC addresses the aforementioned questions, with the novelty being three-fold:

1. To make the procedure readily accessible to practitioners, we employ a dimensionally reduced order model (ROM).
2. To handle nonlinear radiation, we ensure that the variation in the surface temperature obtained via IR imaging is small under the applied heat flux such (i.e., nearly uniform) such that a single value for the combined HTC is representative of heat transfer across the entire surface.
3. To simultaneously estimate the heat transfer coefficient and boundary loss, we avail both the transient and steady-state regimes of thermal response.

3. Parametric estimation framework

3.1. Reduced-order model

In the absence of mechanical work interactions, the first law of thermodynamics applied to our model system (heater, base plate, lateral and bottom insulation) states that the heat input must be equal to the heat exiting. Heat leaves the system primarily through natural convection and radiation from the top surface of the base plate, which is exposed to the ambient atmosphere. Because the materials used to insulate the bottom and lateral surfaces are not perfect insulators, heat is also lost through these surfaces by conduction (i.e., boundary heat loss). The balance of energy applied to the system under these heat transfer interactions takes the form:

$$q_{\text{in}} = q_{\text{tr}}(t) + q_{\text{conv}} + q_{\text{rad}} + q_{\text{loss}}, \tag{1}$$

in which $q_{\text{tr}}(t)$ represents the transient heat transfer to the base plate that produces an increase in temperature. When the system reaches steady state, (i.e., the temperature of the base plate no longer increases), the heat input (q_{in}) is balanced by the heat output represented by the other three terms in Eq. (1), namely the heat loss occurring by convection (q_{conv}), radiation (q_{rad}), and the conductive boundary heat loss (q_{loss}).

Heat flow responsible for the base plate temperature increase in the transient regime is a function of its heat capacity, governed by the material density (ρ), specific heat (c_p) and thickness (d). Since the base plate possess high thermal conductivity, has small thickness relative to its in-plane dimensions, and is subjected to nearly uniform heating, the temperature field in the base plate is expected to be approximately spatially uniform. The surface temperature distribution shown in Fig. 1b supports this approximation. Therefore, the transient term can be described by the equation:

$$q_{\text{tr}}(t) = \rho\, c_p\, d\, \frac{\mathrm{d}T}{\mathrm{d}t}, \tag{2}$$

involving an ordinary derivative for an incremental change in the temperature $\mathrm{d}T$ over a time interval of $\mathrm{d}t$.

Natural convection from the top surface of the base plate to the atmosphere is governed by Newton's law of cooling, which linearly relates the convective heat loss to the difference in temperature between the average top surface temperature (T) and the free stream (ambient) temperature (T_{amb}) through the convective heat transfer coefficient h_{conv} as given by the expression:

$$q_{\text{conv}} = h_{\text{conv}}\,(T - T_{\text{amb}}). \tag{3}$$

Radiative heat loss from the top surface is described by the nonlinear Stefan–Boltzmann equation:

$$q_{\text{rad}} = \varepsilon\, \sigma\, (T^4 - T_{\text{amb}}^4), \tag{4}$$

in which ε is the top surface emissivity and $\sigma \approx 5.67 \times 10^{-8}\ \mathrm{W/(m^2\,K^4)}$ is the Stefan–Boltzmann constant.

Eq. (4) can be factorized into the form:

$$\begin{aligned} q_{\text{rad}} &= \varepsilon\, \sigma\, [(T^2 + T_{\text{amb}}^2)(T + T_{\text{amb}})]\,(T - T_{\text{amb}}) \\ &= h_{\text{rad}}\,(T - T_{\text{amb}}), \end{aligned} \tag{5}$$

that resembles the form of convective heat loss given by Eq. (3), and the two modes can jointly be described by a single linear equation given by:

$$q_{\text{conv+rad}} = h_{\text{comb}}\,(T - T_{\text{amb}}), \tag{6}$$

in which h_{comb} is the combined heat transfer coefficient, given by the expression:

$$h_{\text{comb}} = h_{\text{conv}} + \varepsilon\, \sigma\, (T^2 + T_{\text{amb}}^2)\,(T + T_{\text{amb}}). \tag{7}$$

The use of h_{comb} makes the governing equation amenable to convenient mathematical treatment.

Heat loss occurring by conduction (q_{loss}) through the bottom and lateral insulation is driven by the spatial temperature gradient across these materials. Temperature gradients occur in the insulation because one surface is in contact with the heated base plate, while the rest of the surfaces are cooler being exposed to the atmosphere. Since the base plate temperature evolves with time, the temperature gradient

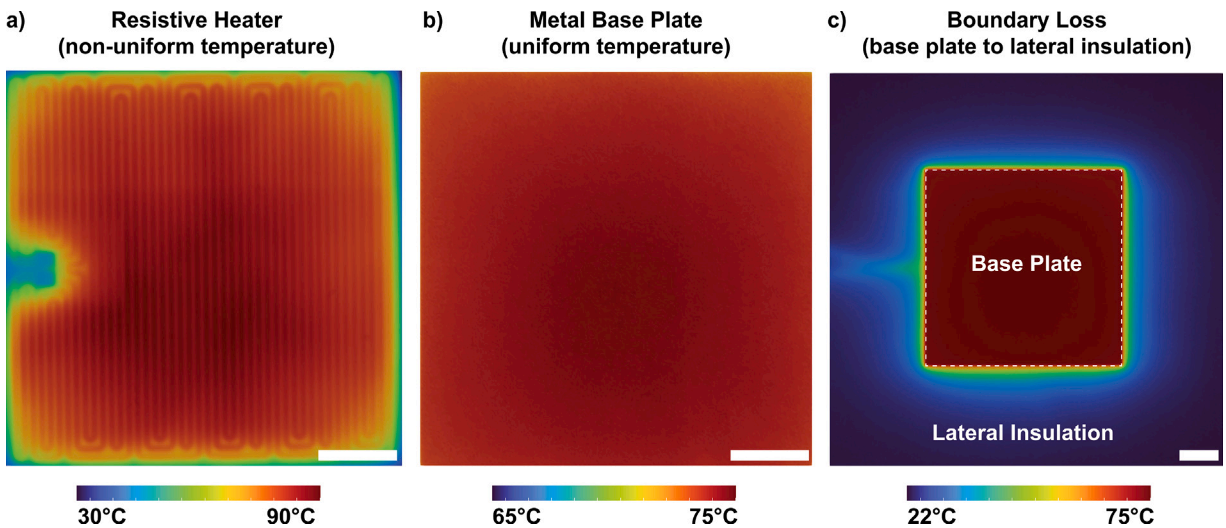

Fig. 1. Experimentally measured top surface temperature contours. (a) Non-uniform temperature field generated by the serpentine resistive heater without a base plate, in contrast to (b) uniform temperature field resulting from a metal base plate placed atop the heater. (c) Temperature contour of the base plate insulated along the lateral sides, in which the temperature gradient from the warmer central region within the dashed square (i.e., base plate) to the cooler sides (i.e., lateral insulation) is indicative of conductive boundary heat loss (scale bars: 20 mm).

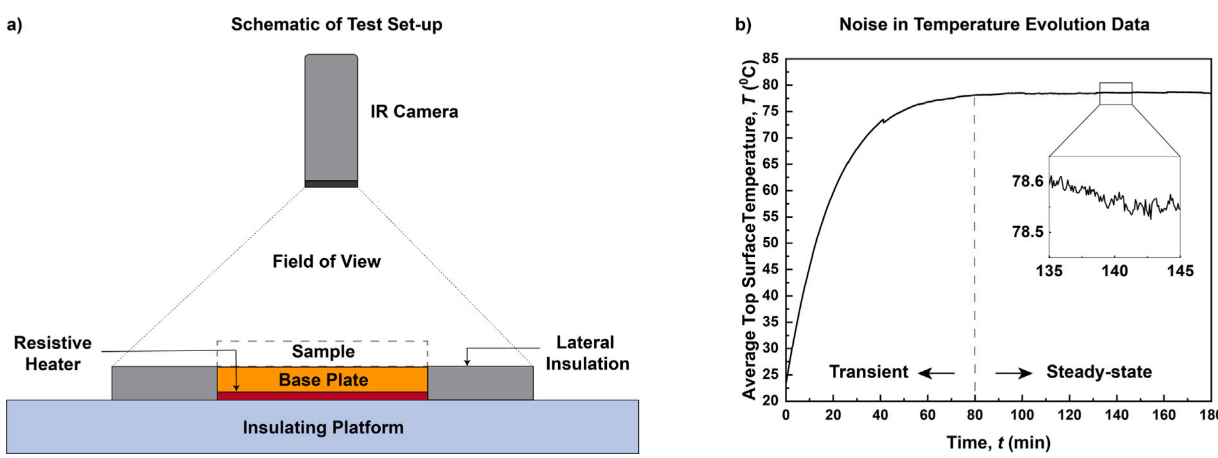

Fig. 2. Elements of an experimental active-cooling study. (a) Schematic of the set-up showing the base plate-resistive heater assembly placed on an insulating platform, and with its lateral sides also insulated. (b) Average top surface temperature evolution of a 6 mm thick copper base plate for an applied heat flux of 1000 W/m^2. The plot shows the temperature evolution recorded by an IR camera through the transient and steady-state regimes, while the inset shows the associated noise in thermal measurements.

responsible for conductive heat loss is also a function of time, i.e., $q_{\text{loss}} = q_{\text{loss}}(t)$.

The conductive boundary loss is governed by Fourier's law at the field level, before spatial reduction. Let $\theta(\mathbf{x}, t)$ denote the local temperature field in the insulation, and let $\mathbf{q}''_{\text{cond}}(\mathbf{x}, t)$ denote the local conductive heat flux. Then

$$\mathbf{q}''_{\text{cond}}(\mathbf{x}, t) = -\mathbf{K}\nabla\theta(\mathbf{x}, t). \tag{8}$$

in which $\mathbf{K}$ is the second-order thermal conductivity tensor of the sample.

The quantity appearing in the reduced-order energy balance is not this local flux, but the spatially integrated boundary loss:

$$q_{\text{loss}}(t) = \int_{\Gamma_{\text{loss}}} \hat{\mathbf{n}} \cdot \mathbf{q}''(\mathbf{x}, t)\, \mathrm{d}\Gamma = -\int_{\Gamma_{\text{loss}}} \hat{\mathbf{n}} \cdot \mathbf{K}\nabla\theta(\mathbf{x}, t)\, \mathrm{d}\Gamma. \tag{9}$$

Here, Γ_{loss} denotes the lateral and bottom loss boundaries, and $\hat{\mathbf{n}}$ is the outward unit normal. After this spatial integration, $q_{\text{loss}}(t)$ becomes a lumped heat-loss term. Likewise, $T(t)$ in the reduced-order model denotes the spatially averaged base-plate temperature. Therefore, Fourier's law is applied to the local temperature field $\theta(\mathbf{x}, t)$ prior to spatial averaging, whereas the reduced-order energy balance is written in terms of the lumped quantities $T(t)$ and $q_{\text{loss}}(t)$.

Using these expressions for the respective heat transfer components, the energy balance Eq. (1) can now be re-written as:

$$q_{\text{in}} = \rho\, c_p\, d\, \frac{\mathrm{d}T(t)}{\mathrm{d}t} + h_{\text{comb}}\,(T(t) - T_{\text{amb}}) + q_{\text{loss}}(t), \tag{10}$$

or equivalently as:

$$\frac{\mathrm{d}T}{\mathrm{d}t} + \frac{h_{\text{comb}}}{\rho\, c_p\, d}\,(T - T_{\text{amb}}) = \frac{q_{\text{in}} - q_{\text{loss}}}{\rho\, c_p\, d} \tag{11}$$

with the initial condition:

$$T = T_{\text{amb}} \quad \text{at} \quad t = 0. \tag{12}$$

Defining $(T - T_{\text{amb}}) = \hat{T}$, these equations reduce to:

$$\frac{\mathrm{d}\hat{T}}{\mathrm{d}t} + \frac{h_{\text{comb}}}{\rho\, c_p\, d}\hat{T} = \frac{q_{\text{in}} - q_{\text{loss}}}{\rho\, c_p\, d} \tag{13}$$

with the corresponding initial condition:

$$\hat{T} = 0 \quad \text{at} \quad t = 0. \tag{14}$$

3.2. Non-dimensionalizing the governing equation

Realistic changes in temperature are expected to occur over the order of minutes, i.e., 10^2 s, and steady-state is achieved for the test cases presented here in ≈3 h, i.e., 10^4 s. On the other hand, the terms $\frac{h_{\rm comb}}{\rho c_p d}$ and $\frac{q_{\rm in}-q_{\rm loss}}{\rho c_p d}$ are on the order of 10^{-3} and 10^{-2}, respectively for our chosen base plate materials and thicknesses. This large difference in the order of the terms (from 10^{-3} to 10^4) involved in Eq. (13) is expected to create numerical instabilities. The issue can be circumvented by non-dimensionalizing the variables, both independent and dependent. The range of the variables can then be restricted to an arbitrarily small value based on the choice of the reference variables chosen for the non-dimensionalization.

Defining the non-dimensionalized (ND) temperature $\bar{T}$ and the ND time $\bar{t}$ as:

$$\bar{T} = \frac{\hat{T}}{T_{\rm amb}}\ ,\ \bar{t} = \frac{t}{t_{\rm ref}}, \tag{15}$$

the governing differential equation becomes:

$$\frac{{\rm d}\bar{T}}{{\rm d}\bar{t}} + \bar{h}_{\rm comb}\,\bar{T} = \bar{q}(\bar{t}), \tag{16}$$

with the initial condition:

$$\bar{T} = 0 \ \text{ at } \ \bar{t} = 0, \tag{17}$$

in which

$$\bar{h}_{\rm comb} = \frac{h_{\rm comb}\,t_{\rm ref}}{\rho\,c_p\,d}, \tag{18}$$

and

$$\bar{q}(\bar{t}) = \frac{(q_{\rm in} - q_{\rm loss}(t))}{\rho\,c_p\,d}\,\frac{t_{\rm ref}}{T_{\rm amb}}. \tag{19}$$

The exercise reveals that the transient thermal response of the system depends on two non-dimensional number groups given by Eqs. (18) and (19). The first of these $\bar{h}_{\rm comb}$ governs the dependence of the temperature on the combined heat transfer coefficient ($h_{\rm comb}$) while the second $\bar{q}(\bar{t})$ shows its dependence on the applied input heat flux ($q_{\rm in}$) as well as boundary heat loss ($q_{\rm loss}$). Both of these number groups are influenced by the heat capacity of the base plate, which is a function of the material (density and specific heat) and geometry (thickness). The choice of the normalization reference time ($t_{\rm ref}$) is arbitrary. In this study, $t_{\rm ref}$ is chosen to be $t_{\max/2}$, where $t_{\max}$ is the duration of the experiment, so that the time axis always spans from 0 to 2. The mathematical decoupling of the heat transfer coefficient and boundary loss terms provides the basis for analyzing the influence of the other parameters on both these quantities, simultaneously, and also informs the choice of a solution strategy for the governing equation (16).

3.3. Parameterization of boundary loss

The complete solution to the first order ordinary differential equation (16) is the sum of the general solution to the homogeneous form of the same equation and the particular integral subjected to the initial condition (17).

As noted earlier, $h_{\rm comb}$ may vary spatially and temporally. However, $h_{\rm comb}$ over the free surface may be time-averaged for the duration of the experiment to obtain a single, constant value for each test, in which case the general solution of the homogeneous equation is given by:

$$\bar{T}^{(h)} = A\,e^{-\bar{h}_{\rm comb}\,\bar{t}}, \tag{20}$$

in which $\bar{h}_{\rm comb}$ is the corresponding non-dimensionalized HTC.

In order to completely determine the solution of (16), we approximate the particular integral by a polynomial series, that is,

$$\bar{T}^{(p)} = \sum_{i=0}^{n} b_i\,t^i, \tag{21}$$

so that:

$$\bar{T} = \bar{T}^{(h)} + \bar{T}^{(p)} = A\,e^{-\bar{h}_{\rm comb}\,\bar{t}} + \sum_{i=0}^{n} b_i\,\bar{t}^i. \tag{22}$$

Using the initial condition (17), we obtain $A = -b_0$, giving:

$$\bar{T} = -b_0\,e^{-\bar{h}_{\rm comb}\,\bar{t}} + \sum_{i=0}^{n} b_i\,t^i. \tag{23}$$

Substituting the above generalized complete solution into the governing differential equation (16), we get the following general expression for the ND boundary heat loss:

$$\bar{q} = \sum_{i=0}^{n} a_i\,t^i, \tag{24}$$

in which

$$a_n = \bar{h}_{\rm comb}\,b_n \tag{25a}$$

$$a_i = (i+1)\,b_{i+1} + \bar{h}_{\rm comb}\,b_i \quad i = n-1, \ldots, 0. \tag{25b}$$

We expect the boundary heat loss to be a nonlinear function of time in keeping with what one might obtain from a conductive, dissipative phenomenon. Therefore, we select a quadratic polynomial form for the particular integral. With this choice, the expression for the ND temperature can be written as:

$$\bar{T} = -b_0\,e^{-\bar{h}_{\rm comb}\,\bar{t}} + b_0 + b_1\,\bar{t} + b_2\,\bar{t}^2. \tag{26}$$

This complete solution consisting of the exponential term combined with a quadratic polynomial was determined to be the simplest adequate representation of the observed temperature evolution, avoiding the need to include higher order terms while preserving the quality of the fit.

By definition, steady state is achieved when the temperature does not vary with time (i.e., $d\bar{T}/d\bar{t} = 0$). If this condition is enforced, the number of unknown constants can be reduced through the additional equation:

$$b_1 = -b_0\,\bar{h}_{\rm comb}\,e^{-\bar{h}_{\rm comb}\,\bar{t}} - 2\,b_2\,\bar{t}. \tag{27}$$

The evolution of the ND temperature field ($\bar{T}$) with ND time ($\bar{t}$) can therefore be described by the equation:

$$\bar{T} = b_0\,[1 - e^{-\bar{h}_{\rm comb}\,\bar{t}}\,(1 + \bar{h}_{\rm comb}\,\bar{t})] - b_2\,\bar{t}^2, \tag{28}$$

involving three unknown parameters, $\bar{h}_{\rm comb}$, b_0 and b_2.

The values of these parameters are obtained by curve fitting the above analytical solution through the temperature evolution data obtained from experiments conducted on base plates with known material/geometric properties (and therefore known heat capacity). However, the experimental data is noisy and needs to be filtered to obtain a smooth temperature evolution, which facilitates an accurate curve fit to the analytical form.

3.4. Filtering experimental temperature evolution data

As noted earlier, temperature data from IR thermography is prone to fluctuations (i.e., noise) due to factors such as electronic drift. A better representation of the actual temperature evolution can be obtained by a smooth mean-value curve drawn through the small-scale noise. Although ensemble averaging of repeated experiments can reduce uncorrelated random noise and is useful for assessing repeatability, the present method is designed for single-transient thermal measurements, where repeated experiments under identical heating and boundary conditions are often impractical or unavailable. Therefore, the measured temperature history from each individual experiment must be processed directly. In this work, a Savitzky–Golay (Savgol) filter [60–63] is used to suppress high-frequency fluctuations in the IR temperature signal while preserving the underlying transient trend. This smoothing

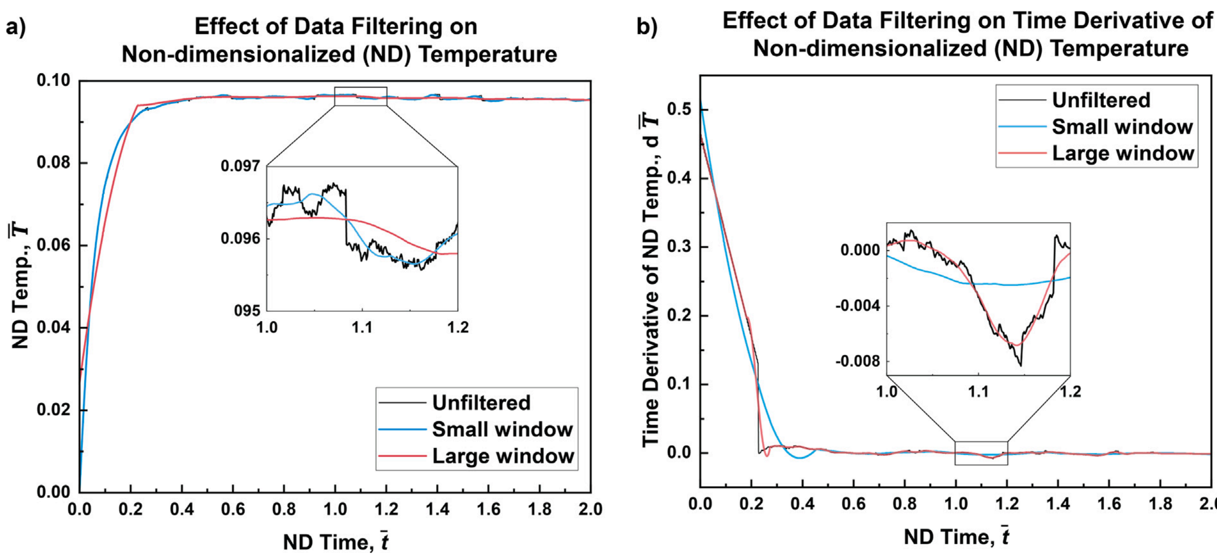

Fig. 3. Digital filtering of experimental data using a Savgol filter [60]. Influence of sampling window size on smoothing of (a) experimental temperature evolution data, and (b) its derivative with respect to time.

step is particularly important because the subsequent estimation procedure requires numerical differentiation of the temperature–time data, and differentiation can otherwise amplify high-frequency measurement noise.

The Savgol filter considers a sampling window of a specified number of data points, through which a polynomial of a specified order is fit to compute an average value at the center of the window. The algorithm provides a smoothed curve drawn through these moving window averages. While the window size must be a positive, odd number, there are no strict rules on the exact value to be chosen. The general recommendation is that the window size span 1–2 times the full width at half maximum. In our experiment, we gather temperature values approximately every 5 s. The base plate can take anywhere between 20 to 80 min to achieve steady state, depending on the heat capacity of the plate. Half this change occurs over a span of 10 to 40 min (120 to 480 data points). Therefore, we select window sizes on either side of this limit, consisting of 101 and 501 data points, respectively. The smoothed curve calculated using these window sizes is expected to serve as a faithful representation of the theoretically predicted curve (28), which consists of an exponential and a quadratic component. Hence, we investigate these window sizes coupled with a second order polynomial fit for the filtering algorithm.

Fig. 3a shows the curve fit obtained using small (101) and large (501) window sizes for the ND mean temperature obtained from IR camera measurements on a 2 mm aluminum base plate with an input heat flux of 500 $\mathrm{W/m^2}$. The large window produces a smoother curve albeit at the expense of not capturing the finer behavior at the time scale shown in the inset. Note, for our choice of $t_{\mathrm{ref}} = t/2$, ND time ($\bar{t}$) of 0.1 translates to actual time (t) of 9 min. Since we expect temperature variations at this time scale to be realistic, we seek a smoothed curve that captures variations at this scale accurately. The small (101) window fares better in this regard.

Plotting the time derivative of the ND temperature brings forth another aspect, where in Fig. 3b a distinct change in slope can be seen at the transition from transient to steady-state. As shown in this comparison, the large window captures the slope change better than the small window. Thus, there is an interplay between window size and the time scale of the fluctuations being smoothed. Temperature evolution during the transient regime and through the transition to the steady-state occurs over the time scale of tens of minutes. However, thermal noise from the IR camera (that we seek to filter) occurs at a time scale at least one order of magnitude lower. Hence, we select the Savgol filter with a small (101) size window to obtain a smooth, realistic surface temperature evolution.

3.5. Estimation of boundary heat loss

After the experimental temperature evolution data is non-dimensionalized (ND) and smoothed, the theoretical curve given by Eq. (28) is fit to the data, allowing for the three parameters identified earlier ($\bar{h}_{\mathrm{comb}}$, b_0, b_2) to be optimized for the best fit. The combined HTC in dimensional form can then be readily obtained using Eq. (18).

To compute the boundary heat loss, we substitute the analytical solution (28) into the governing differential equation (16) to obtain:

$$\bar{q} = (b_1 + \bar{h}_{\mathrm{comb}}\, b_0) + (2\, b_2 + \bar{h}_{\mathrm{comb}}\, b_1)\, \bar{t} + \bar{h}_{\mathrm{comb}}\, b_2\, \bar{t}^2, \tag{29}$$

which can be written as:

$$\bar{q} = a_0 + a_1\, \bar{t} + a_2\, \bar{t}^2, \tag{30}$$

in which

$$a_0 = b_1 + \bar{h}_{\mathrm{comb}}\, b_0, \tag{31a}$$

$$a_1 = 2\, b_2 + \bar{h}_{\mathrm{comb}}\, b_1, \tag{31b}$$

$$a_2 = \bar{h}_{\mathrm{comb}}\, b_2. \tag{31c}$$

We observe that these relations can also be equivalently derived from Eqs. ((25)a,b) by choosing $n = 2$, which represents a quadratic form of the particular solution to the ND temperature field.

We also have an expression for $\bar{q}$ from Eq. (19). Equating these two expressions, we obtain the following relation for boundary heat loss:

$$q_{\mathrm{loss}} = q_{\mathrm{in}} - \frac{\rho\, c_p\, d\, T_{\mathrm{amb}}}{t_{\mathrm{ref}}}\,(a_0 + a_1\, \bar{t} + a_2\, \bar{t}^2). \tag{32}$$

This expression is used in subsequent investigations to calculate the boundary loss for different base plate materials, thicknesses, and lateral and bottom surface insulation materials and geometries.

Fig. 2b,c show that the temperature field near the boundary is not spatially uniform, indicating a non-zero temperature gradient normal to the boundary. Therefore, the conductive heat flux through the boundary is not zero, and the assumption of a perfectly adiabatic boundary can introduce systemic error. In the proposed formulation, the boundary heat loss is estimated directly rather than neglected. The estimated boundary loss term corresponds to the integral of the conductive heat flux over the boundary and is consistent with the conductive-loss estimate obtained from Fourier's law given by Eq. (9) using the measured boundary temperature gradients. Thus, the proposed method provides a more physically accurate estimate of the combined HTC by accounting for boundary losses that are ignored under the conventional adiabatic-boundary assumption.

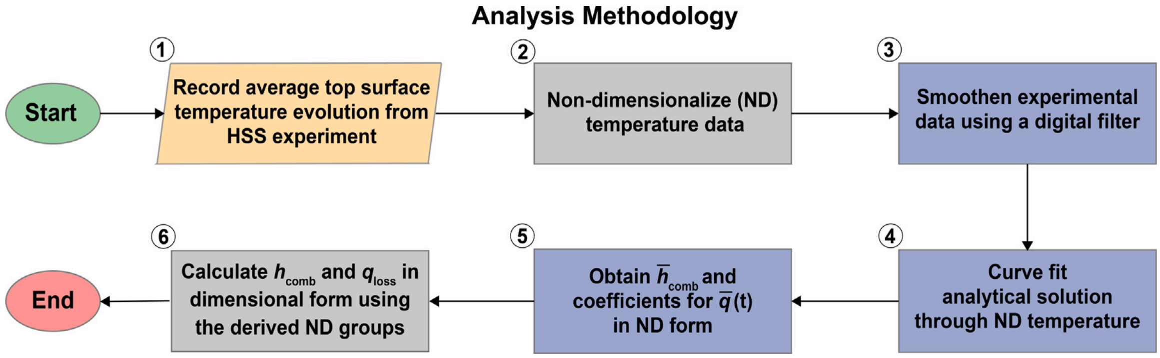

Fig. 4. Flowchart of the analysis sequence. The six step procedure utilizes experimental input (temperature evolution data), analytical techniques (non-dimensionalization and theoretical solution), as well as numerical strategies (data filtering and curve fitting) to simultaneously estimate combined HTC (h_{comb}) and boundary heat loss (q_{loss}).

4. Experimental methodology

Two high conductivity metals—Copper 110 (isotropic thermal conductivity, κ = 385.58 W/(m K); density, ρ = 8843 kg/m^3; specific heat, c_p = 390.88 J/(kg K)) and Aluminum 6061 (κ = 173.46 W/(m K), ρ = 2669 kg/m^3, c_p = 923.83 J/(kg K))) were chosen as candidate materials for the base plate. This was based on the requirement that the 100 × 100 mm base plate needs to possess high thermal conductivity to even out the non-uniform heat flux emanating from the serpentine metal pattern in the thin film resistive heater (Omega, KH608/2) underneath. In a typical active-cooling experiment, a test sample (e.g., containing internal vasculature) is mounted atop the base plate forming the topmost layer as shown in Fig. 2a. However, because the present study focuses on quantifying boundary effects extraneous to the sample, the setup here does not include the sample itself. Three different thicknesses (d ≈ 2, 4, 6 mm) of each base plate material were evaluated for influence on combined HTC and boundary loss. In order that the top surface of the base plates which are placed on the heater (≈ 0.15 mm thick) be flush with standard lateral insulation thicknesses of 2, 4 and 6 mm, the plates were machined down by 0.2 mm, resulting in the actual thicknesses of 1.8, 3.8 and 5.8 mm. For convenience however, the original plate thicknesses (d) of 2, 4 and 6 mm are referred to in subsequent sections.

High density ethylene-vinyl acetate (EVA) foam (κ = 0.03 W/(m K)) was selected as the lateral insulation. EVA sheets of the three chosen thicknesses were laser cut into 200 × 200 mm squares. Concentric 100 × 100 mm square cut-outs matching the areal dimension of each base plate were then laser cut into the EVA foam to obtain flat, snugly fitting lateral insulation for each base plate. The layered assembly (base plate, heater, lateral insulation) was then placed on an insulating platform measuring ≈305 × 305 × 25 mm.

Two platform insulation materials were used in this study to assess the impact of axial insulation on boundary heat loss: (i) balsa wood, and (ii) polyisocyanurate (PIR) foam. While balsa wood is a common material used in prior active-cooling experiments [26–28], it is inherently anisotropic, leading to non-uniform insulating behavior, which is both undesirable and difficult to quantify. PIR foam, on the other hand, is a rigid, closed-cell foam that is isotropic and has a lower thermal conductivity (κ = 0.027 W/(m K)) than balsa wood (κ = 0.03 to 0.06 W/(m K)), making it a stronger contender for the insulation platform. Various combinations of base plate materials and thicknesses were placed on each of these two platforms, and boundary heat loss was evaluated for applied heat fluxes of 500, 1000, 1500 and 2000 W/m^2.

Evolution of the average top surface temperature, henceforth denoted by $\tilde{T}$, was tracked using an IR camera (FLIR, A655sc) at an image sampling rate of 0.2 Hz. The base plates were spray painted matte black to avoid reflections into the overhead mounted IR camera. The assembly was heated from below via the resistive heater with constant electric power input, that was dynamically adjusted for heater resistance changes during the experiment, thereby ensuring constant heat flux to reach hot steady state (HSS). Because $\tilde{T}$ is expected to asymptotically approach its steady state value ($\tilde{T}_{HSS}$), a criterion suitable for experimental identification of HSS was deemed when $\tilde{T}$ varied by less than ±0.2 °C [28,37]. The ambient temperature was kept approximately the same across all experiments at 22 ± 0.5 °C. The emissivity (≈0.94) of the painted top surface of both base plate materials was measured according to ASTM standard E1933-14 across the range of heat fluxes selected [38]. The evolution of $\tilde{T}$ through transient and steady-state regimes was then studied varying four parameters: (i) applied heat flux, (ii) thickness of the base plate, (iii) its thermal conductivity, and (iv) the thermal conductivity of the platform insulation. The impact of these four variables on h_{comb} and q_{loss} are detailed in the following section.

5. Analysis and results

Fig. 4 shows the six step sequence for the simultaneous estimation of h_{comb} and q_{loss}: ① HSS experiments are conducted on each combination of the variables (i–iv) chosen for this study from which the evolution of average top surface temperature ($\tilde{T}$) is obtained; ② The data is then non-dimensionalized (ND) and recast as the evolution of the corresponding ND average top surface temperature ($\bar{T}$) with ND time ($\bar{t}$); ③ Thereafter, the noise in the data is filtered using a digital data filter (e.g., Savgol) with appropriately chosen parameters that allow for an accurate, smooth trace of the ND data to be obtained; ④ The analytical solution for the evolution of ND temperature derived earlier in Section 3 and given by Eq. (28) is then curve fit through the smoothed data, from which ⑤ the optimized values of the three unknown parameters $\bar{h}_{comb}$, b_0, b_2 are obtained. ⑥ From these, coefficients a_0, a_1 and a_2—required to back calculate h_{comb} and q_{loss} in dimensional form—are obtained as given by Eqs. ((31)a–c). The value of h_{comb} and q_{loss} in dimensional form are then calculated from Eqs. (18) and (32). The influence of the chosen parameters on the evolution of average top surface temperature, h_{comb}, and q_{loss} are then analyzed to reveal the following results.

5.1. Average top surface temperature trends

The transient temperature evolution curves for 6 mm thick copper and aluminum plates placed on balsa wood and foam platforms are shown in Fig. 5a and b, respectively. The curves show that the temperature rises exponentially in the transient regime, eventually achieving a nearly constant value in steady state. This agrees with the analytical solution for the ND temperature ($\bar{T}$) evolution given by Eq. (28), with ND time ($\bar{t}$) and $\bar{h}_{comb}$ being positive quantities. The curves clearly indicate that higher applied heat fluxes lead to higher top surface

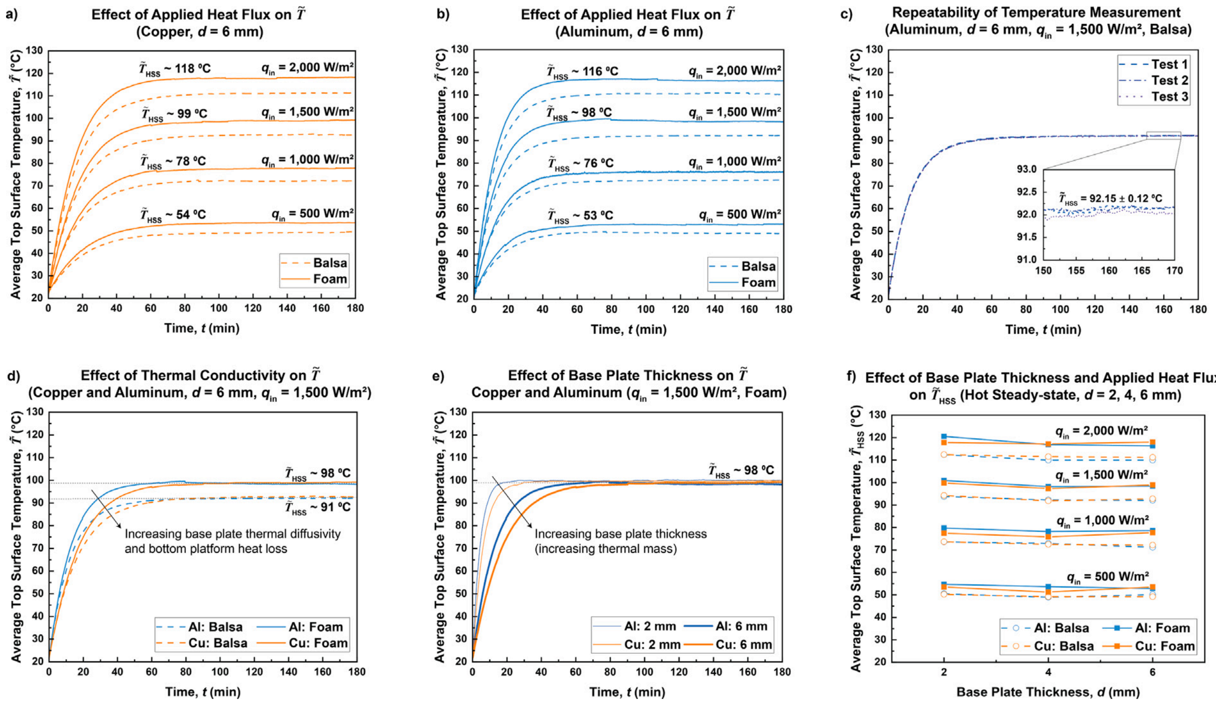

Fig. 5. Average top surface temperature ($\tilde{T}$) evolution. Effect of applied heat flux and base platform insulation on $\tilde{T}$ for (a) copper and (b) aluminum base plates of 6 mm thickness. (c) Temperature evolution curves for three repeat experiments conducted on a 6 mm aluminum base plate placed on a balsa wood platform. (d) Effect of base plate thermal conductivity and base platform insulation on $\tilde{T}$ at a given plate thickness (6 mm) and applied heat flux (1500 W/m^2). (e) Effect of base plate thickness on $\tilde{T}$ at an applied heat flux of 1500 W/m^2 for a foam platform. (f) Hot steady-state average top surface temperature ($\tilde{T}_{HSS}$) for different base plate materials, thicknesses, applied heat fluxes and platform insulation.

temperatures. Also apparent is that the slope of the transient curve increases with the applied heat flux, conforming to the theoretical prediction given by Eq. (2). Furthermore, the data also shows that the use of PIR foam as the platform insulation leads to higher surface temperatures than balsa wood, indicating that foam has lower overall heat loss and is indeed a better choice for insulation.

Since the proposed methodology is based on fitting the derived mathematical model through experimental temperature evolution curves, it is important to ensure reliability of temperature data from IR camera measurements. To assess, we select the case of a 6 mm aluminum base plate on a balsa wood platform with an applied heat flux of 1500 W/m^2. Fig. 5c shows the temperature evolution curves for three such experiments with overlapping curves across both transient and steady-state regimes, with the mean steady-state top surface temperature being 92.15 °C and associated standard deviation of ±0.12 °C. The small standard deviation (below IR camera precision [37]) together with the close spacing of the three curves in transient as well as steady-state regimes, demonstrates experimental repeatability and fidelity in temperature measurements.

Fig. 5d shows the influence of the base plate thermal diffusivity (ratio of thermal conductivity, κ to volumetric heat capacity, ρc_p) on the transient temperature rise. As expected, the higher thermal diffusivity copper climbs at a slower rate to reach steady state than aluminum. Additionally, Fig. 5d indicates a weak dependence of the steady-state average top surface temperature ($\tilde{T}_{HSS}$) on the diffusivity of the base plate. According to Fourier's law of heat conduction given by Eq. (9), but now applied to the base plate, the difference in temperature between the bottom and top faces of a 6 mm base plate for an applied heat flux of 1500 W/m^2 is ≈0.02 °C for copper and ≈0.05 °C for aluminum.

Fig. 5e highlights the role of base plate thickness on temperature evolution, especially in the transient regime, where thinner plates reach steady state faster than thicker ones due to lower thermal mass. However, as shown in Fig. 5f, base plate thickness minimally affects the steady-state average top surface temperature. Based on a similar calculation using Fourier's law as above, the difference in average top surface temperature (for either aluminum or copper) due to thickness change from 2 to 6 mm is on the order of 10^{-2} °C. Thus, the base plate is effective at minimizing through-thickness thermal gradients, validating our use of a dimensionally reduced order model (ROM).

5.2. Effect of applied heat flux

Fig. 6a shows the variation in h_{comb} with applied heat flux, obtained from our experiments on copper and aluminum base plates of 6 mm thickness. Since $\tilde{T}$ increases with applied heat flux (Fig. 5a,b) while the ambient temperature remains approximately the same, the temperature difference (ΔT) increases. This leads to an increase in convective and radiative heat losses from the top surface, and therefore h_{comb} increases with the applied heat flux.

Fig. 6b shows the associated variation of boundary heat loss with applied heat flux. $\tilde{T}$ varies significantly with applied heat flux, while the type of metal and thickness of the base plate did not affect the temperature as strongly (Fig. 5d). This indicates that the amount of heat transferred by both convective and radiative modes increases with applied heat flux. The boundary heat loss, which is the difference between these two simultaneously increasing quantities (i.e., the applied heat flux and the sum of the convective/radiative heat losses) is therefore a weak function of the applied heat flux. However, boundary heat loss shows a strong dependence on platform insulation. As noted earlier, the increase in surface temperature resulting from the use of PIR foam in place of balsa wood points to a smaller amount of heat flowing through the platform insulation, thus naturally leading to lower boundary loss.

5.3. Effect of base plate thickness

As mentioned in Section 5.1, base plate thickness affects the transient response but does not significantly affect the steady-state temperature (Fig. 5e,f). Since h_{comb} is obtained using the temperature evolution

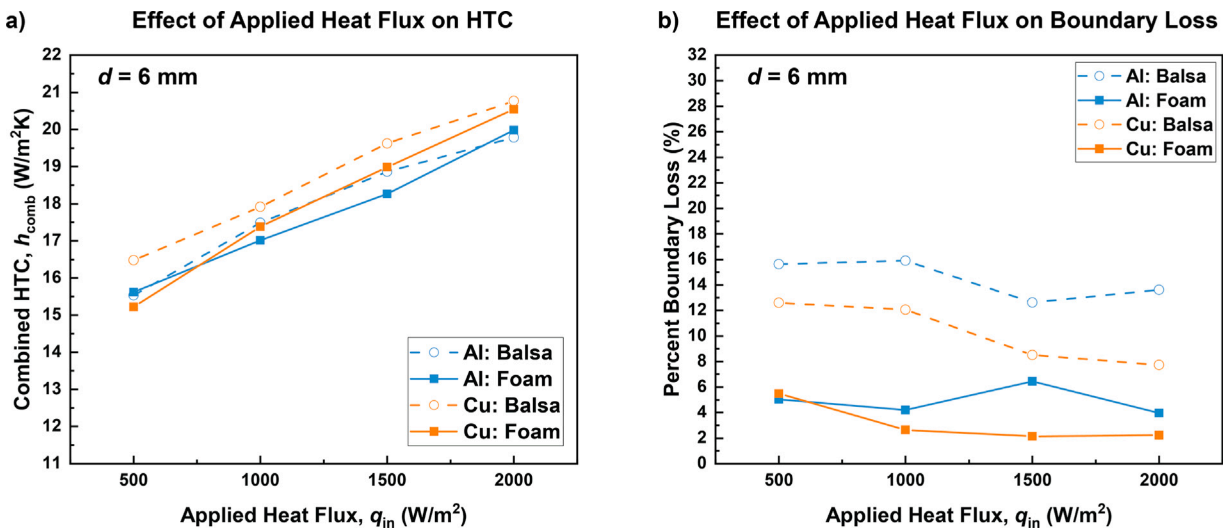

Fig. 6. Effect of applied heat flux. Variation of (a) combined heat transfer coefficient (h_{comb}), and (b) boundary heat loss (q_{loss}), for 6 mm thick base plates.

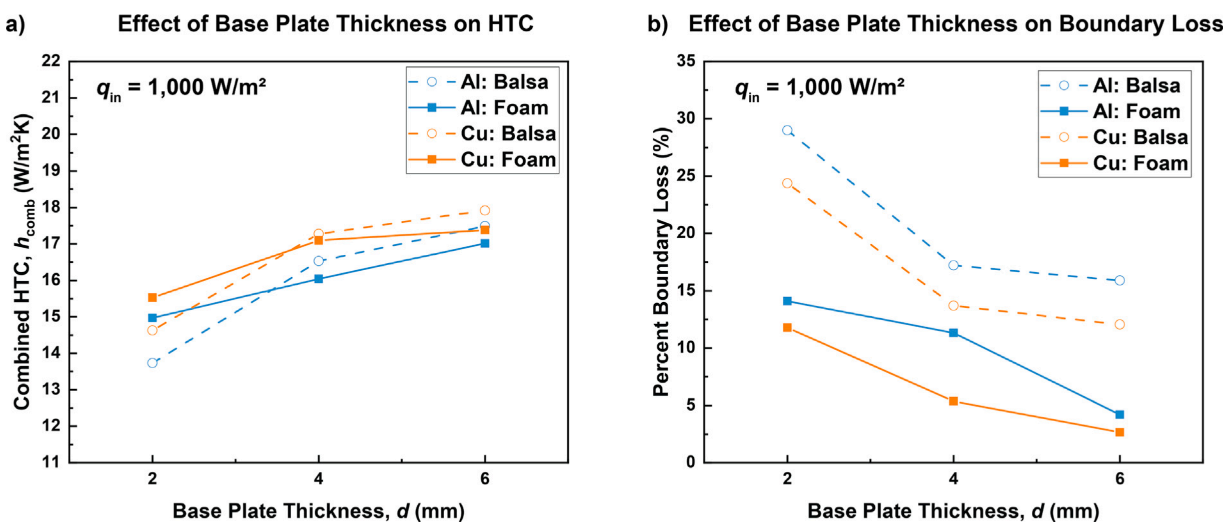

Fig. 7. Effect of base plate thickness. Variation of (a) combined heat transfer coefficient (h_{comb}), and (b) boundary heat loss (q_{loss}), for an applied heat flux of 1000 W/m^2.

curve spanning both, transient as well as steady-state regimes, we expect the combined HTC to be a function of base plate thickness, as shown in Fig. 7a. However, because of its minimal influence on $\tilde{T}_{HSS}$, ΔT between the top surface and the ambient remains approximately the same at steady-state irrespective of base plate thickness at any given heat flux. Since the Stefan–Boltzmann constant and emissivity also remain the same, radiative effects are not expected to change much with plate thickness variations.

Convective effects, on the other hand, are likely to be influenced by a change in base plate thickness. The assembly mimics the classical horizontal flat plate configuration with the hot surface facing upwards. A change in base plate thickness therefore directly translates to a change in step height that the convective currents encounter. Several correlations are available in literature for the convective heat transfer coefficient (h_{conv}) in terms of the geometric parameters and orientation of the solid surface, and the flow properties of the fluid medium. These correlations typically assume the plate to be "thin" in order to predict the nature of variation in h_{conv}, and seldom agree even on fundamental parameters used in these relations. For example, some studies use the length of the short edge as the characteristic length, while others use alternative measures such as the ratio of the surface area to the perimeter [64,65]. In essence, natural convection involving plates of finite thickness are fairly non-trivial, especially on the theoretical front [66,67]. In this light, combined experimental/analytical studies such as the present one offer a convenient and effective alternative to assess these effects. The results from our study indicate that the combined heat transfer coefficient (h_{comb}) increases with base plate thickness, as shown in Fig. 7a. Since radiative effects do not vary, the measured trend points to improved convection with an increase in base plate thickness.

From the energy balance Eq. (1), if the amount of heat transferred by convection increases while that transferred by radiation remains the same for a prescribed applied heat flux and the same lateral and bottom insulation, the proportion of heat lost through these boundaries must reduce. Fig. 7b confirms this logic, with lower boundary losses occurring for higher base plate thicknesses. Again, the data shows that the boundary heat loss is significantly lower with the use of foam as the platform insulation rather than commonly employed balsa wood [26–28].

5.4. Effect of base plate thermal conductivity

Higher thermal conductivity implies better temperature uniformity (i.e., smaller temperature gradients) in every plane normal to the thickness direction, including the top surface. Minimizing in-plane thermal gradients restricts gradients to primarily along the thickness from the heater interface to the top free surface. In turn, this lowers the propensity for planar heat flow, i.e., through the lateral boundaries. Consequently, the boundary loss described by Eq. (9) is expected to be smaller in higher conductivity copper than in aluminum. Boundary loss trends observed earlier in Figs. 6 and 7 corroborate this intricate heat transfer mechanism, shedding new light on thermal behavior for optimizing system-level design.

6. Closure

This paper puts forth an innovative framework—comprising an experimental protocol and parametric modeling—that accurately estimates the convective HTC, accounting for conductive heat loss through imperfectly insulated boundaries. Thus, this hybrid framework provides a solution to the longstanding practice of assuming adiabaticity [29–34], even with imperfectly insulated boundaries, owing in large part to accessible analytical tools not being available. When applied here to the model problem mirroring the experimental setup widely used in microvascular active-cooling studies, the methodology not only allows for simultaneous quantification of these two coupled quantities, but in doing so also reveals the advantage of using thicker base plates of high thermal conductivity to even out non-uniformity in heat flux emanating from an external heat source. Furthermore, the technique also informs the selection of insulating materials by providing accurate quantification of conductive heat losses through the boundary, where our results show less heat transfer occurs with a closed cell polymer foam platform over balsa wood often employed in active-cooling studies [26–28].

We envision several applications for our framework. As an extension applied to the same model problem, the technique can now be used to more finely study thermal regulation of microvascular fiber-composites and metals in layered configurations, e.g., photovoltaics and electric vehicle battery cooling [30,31,52]. Such heterogeneous materials and architectures induce additional intricacy via thermal non-uniformity. For example, complex temperature gradients arising in sandwich structures comprised of materials with different thermal properties and subject to non-uniform heat sources pose significant challenges for estimating the HTC and boundary losses, which can now be conveniently navigated via the framework laid out herein. Thus, we strengthen the understanding required to advance experimental and theoretical thermal regulation research with transferable benefits across a broad landscape of industrial heat transfer applications.

CRediT authorship contribution statement

Sandeep R. Kumar: Writing – review & editing, Writing – original draft, Visualization, Investigation, Formal analysis, Data curation. **Kalyana B. Nakshatrala:** Writing – review & editing, Writing – original draft, Methodology, Investigation, Funding acquisition, Formal analysis, Conceptualization. **Jason F. Patrick:** Writing – review & editing, Visualization, Supervision, Methodology, Investigation, Funding acquisition.

Declaration of competing interest

The authors declare the following financial interests/personal relationships which may be considered as potential competing interests: Kalyana B. Nakshatrala reports financial support was provided by US Army Research Office. If there are other authors, they declare that they have no known competing financial interests or personal relationships that could have appeared to influence the work reported in this paper.

Acknowledgment

This work was supported by the U.S. Army Research Office (ARO) under Contract No. W911NF2510289.

Data availability

The data supporting the findings of this study are available upon request.

References

[1] T.L. Pourpoint, V. Velagapudi, I. Mudawar, Y. Zheng, T.S. Fisher, Active cooling of a metal hydride system for hydrogen storage, Int. J. Heat Mass Transfer 53 (2010) 1326–1332.
[2] K.B. Nakshatrala, K. Adhikari, S.R. Kumar, J.F. Patrick, Configuration-independent thermal invariants under flow reversal in thin vascular systems, PNAS Nexus 2 (8) (2023) pgad266.
[3] M. Shad, X. Zhang, Parametric study of miniature stirling cryocooler for high temperature infrared detector with design refinement for SWaP configuration, Appl. Therm. Eng. 273 (2025) 126495.
[4] H. Fernandes, Overcome thermal-management challenges in rugged-system design to optimize SWaP-C, in: Electronic Design Library: Tackling Thermal Design of Rugged Systems, Endeavor Media, 2024.
[5] T. Fujii, H. Imura, Natural-convection heat transfer from a plate with arbitrary inclination, Int. J. Heat Mass Transfer 14 (1972) 755–767.
[6] S.W. Churchill, H.H. Chu, Correlating equations for laminar and turbulent free convection from a vertical plate, Int. J. Heat Mass Transfer 18 (11) (1975) 1323–1329.
[7] C. Kobus, G. Wedekind, An experimental investigation into forced, natural and combined forced and natural convective heat transfer from stationary isothermal circular disks, Int. J. Heat Mass Transfer 38 (18) (1995) 3329–3339.
[8] A.-J.N. Khalifa, Natural convective heat transfer coefficient–a review: I. Isolated vertical and horizontal surfaces, Energy Convers. Manage. 42 (4) (2001) 491–504.
[9] I. Martorell, J. Herrero, F.X. Grau, Natural convection from narrow horizontal plates at moderate Rayleigh numbers, Int. J. Heat Mass Transfer 46 (13) (2003) 2389–2402.
[10] K. Kitamura, A. Mitsuishi, T. Suzuki, F. Kimura, Fluid flow and heat transfer of natural convection adjacent to upward-facing, rectangular plates of arbitrary aspect ratios, Int. J. Heat Mass Transfer 89 (2015) 320–332.
[11] E. Marín, A. Calderón, O. Delgado-Vasallo, Similarity theory and dimensionless numbers in heat transfer, Eur. J. Phys. 30 (2009) 439.
[12] M.I. Davidzon, Newton's law of cooling and its interpretation, Int. J. Heat Mass Transfer 55 (2012) 5397–5402.
[13] B. Zhao, Integrity of Newton's cooling law based on thermal convection theory of heat transfer and entropy transfer, Sci. Rep. 12 (1) (2022) 16292.
[14] F.P. Incropera, D.P. DeWitt, T.L. Bergman, A.S. Lavine, et al., Fundamentals of Heat and Mass Transfer, Vol. 6, Wiley New York, 1996.
[15] S. Ostrach, Natural convection in enclosures, ASME J. Heat Transf. 110 (1988) 1175–1190.
[16] S. Pandey, Y. Park, M. Ha, An exhaustive review of studies on natural convection in enclosures with and without internal bodies of various shapes., Int. J. Heat Mass Transfer 138 (2019) 762–795.
[17] G. Cesini, P. Massimo, G. Cortella, M. Manzan, Natural convection from a horizontal cylinder in a rectangular cavity, Int. J. Heat Mass Transfer 42 (1999) 1801–1811.
[18] S. Atayılmaz, I. Teke, Experimental and numerical study of the natural convection from a heated horizontal cylinder., Int. Commun. Heat Mass Transfer 36 (7) (2009) 731–738.
[19] A. Baïri, E. Zarco-Pernia, J. De María, A review on natural convection in enclosures for engineering applications. The particular case of the parallelogrammic diode cavity., Appl. Therm. Eng. 63 (2014) 304–322.
[20] J. Claesson, C. Hagentoft, Heat loss to the ground from a building—I. General theory., Build. Environ. 26 (2) (1991) 195–208.
[21] R. de Lieto Vollaro, L. Fontana, A. Quintino, A. Vallati, Improving evaluation of the heat losses from arrays of pipes or electric cables buried in homogeneous soil, Appl. Therm. Eng. 31 (17–18) (2011) 3768–3773.
[22] H.H. Bau, S. Sadhai, Heat losses from a fluid flowing in a buried pipe, Int. J. Heat Mass Transfer 25 (11) (1982) 1621–1629.
[23] A. Kawaguchi, Y. Wakisaka, N. Nishikawa, H. Kosaka, H. Yamashita, C. Yamashita, H. Iguma, K. Fukui, N. Takada, T. Tomoda, Thermo-swing insulation to reduce heat loss from the combustion chamber wall of a diesel engine, Int. J. Engine Res. 20 (7) (2019) 805–816.
[24] B. Hadała, Z. Malinowski, M. Rywotycki, Energy losses from the furnace chamber walls during heating and heat treatment of heavy forgings., Energy 139 (2017) 298–314.

[25] B.D. Kozola, L.A. Shipton, V.K. Natrajan, K.T. Christensen, S.R. White, Characterization of active cooling and flow distribution in microvascular polymers, J. Intell. Mater. Syst. Struct. 21 (12) (2010) 1147–1156.
[26] S.J. Pety, M.H.Y. Tan, A.R. Najafi, P.R. Barnett, P.H. Geubelle, S.R. White, Carbon fiber composites with 2D microvascular networks for battery cooling, Int. J. Heat Mass Transfer 115 (2017) 513–522.
[27] S.J. Pety, P.X. Chia, S.M. Carrington, S.R. White, Active cooling of microvascular composites for battery packaging, Smart Mater. Struct. 26 (10) (2017) 105004.
[28] U. Devi, R. Pejman, Z.J. Phillips, P. Zhang, S. Soghrati, K.B. Nakshatrala, A.R. Najafi, K.R. Schab, J.F. Patrick, A microvascular-based multifunctional and reconfigurable metamaterial, Adv. Mater. Technol. 6 (11) (2021) 2100433.
[29] W. Qu, I. Mudawar, Experimental and numerical study of pressure drop and heat transfer in a single-phase micro-channel heat sink, Int. J. Heat Mass Transfer 45 (12) (2002) 2549–2565.
[30] H. Yao, W. Pu, J. Wang, Y. Qin, L. Qiao, N. Song, A novel thermosyphon cooling applied to concentrated photovoltaic-thermoelectric system for passive and efficient heat dissipation, Appl. Therm. Eng. 236 (2024) 121460.
[31] S. Wang, J. Shi, H.-H. Chen, S.R. Schafer, M. Munir, G. Stecker, W. Pan, J.-J. Lee, C.-L. Chen, Cooling design and evaluation for photovoltaic cells within constrained space in a CPV/CSP hybrid solar system, Appl. Therm. Eng. 110 (2017) 369–381.
[32] R. Pejman, S.H. Aboubakr, W.H. Martin, U. Devi, M.H.Y. Tan, J.F. Patrick, A.R. Najafi, Gradient-based hybrid topology/shape optimization of bioinspired microvascular composites, Int. J. Heat Mass Transfer 144 (2019) 118606.
[33] J. Gorman, R. Pejman, S.R. Kumar, J.F. Patrick, A.R. Najafi, Transient topology optimization for efficient design of actively cooled microvascular materials, Struct. Multidiscip. Optim. 67 (4) (2024) 60.
[34] X. Chen, F.N. Donmezer, S. Kumar, S. Graham, A numerical study on comparing the active and passive cooling of algan/gan HEMTs, IEEE Trans. Electron Devices 61 (12) (2014) 4056–4061.
[35] G.M. Rao, G. Narasimham, Laminar conjugate mixed convection in a vertical channel with heat generating components, Int. J. Heat Mass Transfer 50 (17–18) (2007) 3561–3574.
[36] S. Feng, M. Shi, H. Yan, S. Sun, F. Li, T.J. Lu, Natural convection in a cross-fin heat sink, Appl. Therm. Eng. 132 (2018) 30–37.
[37] U. Devi, S. Kumar, K. Nakshatrala, J. Patrick, A methodology for measuring heat transfer coefficient and self-similarity of thermal regulation in microvascular material systems., Int. J. Heat Mass Transfer 217 (2023) 124614.
[38] ASTM E1933-14. Standard practice for measuring and compensating for emissivity using infrared imaging radiometers, 2018.
[39] J.P. Johnston, J.M. Pereira, C.R. Ruggeri, G.D. Roberts, High-speed infrared thermal imaging during ballistic impact of triaxially braided composites, J. Compos. Mater. 52 (25) (2018) 3549–3562.
[40] S. Soudian, U. Berardi, N. Laschuk, Development and thermal-optical characterization of a cementitious plaster with phase change materials and thermochromic paint, Sol. Energy 205 (2020) 282–291.
[41] U. Berardi, M. Garai, T. Morselli, Preparation and assessment of the potential energy savings of thermochromic and cool coatings considering inter-building effects, Sol. Energy 209 (2020) 493–504.
[42] A.I. Savadelis, J.M. Pereira, B.E. Schmidt, Transient temperature measurements in a ballistic impact experiment on a thermoplastic composite material, Compos. Part B: Eng. 295 (2025) 112157.
[43] J. Beck, K. Arnold, Parameter Estimation in Engineering and Science, in: International series of monographs on physics, John Wiley & Sons, 1977.
[44] R.C. Aster, B. Borchers, C.H. Thurber, Parameter Estimation and Inverse Problems, Elsevier, 2018.
[45] R. Das, S.C. Mishra, T.P. Kumar, R. Uppaluri, An inverse analysis for parameter estimation applied to a non-Fourier conduction–radiation problem, Heat Transf. Eng. 32 (6) (2011) 455–466.
[46] M. Lazard, S. Andre, D. Maillet, A. Degiovanni, Radiative and conductive heat transfer: a coupled model for parameter estimation., High Temperatures–High Press. 32 (1) (2000) 9–17.
[47] K. Cole, C. Tarawneh, B. Wilson, Analysis of flux-base fins for estimation of heat transfer coefficient., Int. J. Heat Mass Transfer 52 (1–2) (2009) 92–99.
[48] N. Gnanasekaran, C. Balaji, A Bayesian approach for the simultaneous estimation of surface heat transfer coefficient and thermal conductivity from steady state experiments on fins., Int. J. Heat Mass Transfer 54 (13–14) (2011) 3060–3068.
[49] T. Zawada, Simultaneous estimation of heat transfer coefficient and thermal conductivity with application to microelectronic materials., Microelectron. J. 37 (4) (2006) 340–352.
[50] M. Malavasi, L. Cattani, P. Vocale, F. Bozzoli, S. Rainieri, Thermal characterisation of triple tube heat exchangers by parameter estimation approach., Int. J. Heat Mass Transfer 178 (2021) 121598.
[51] A. Driesman, J. Ercol, E. Gaddy, A. Gerger, Journey to the center of the solar system: how the Parker solar probe survives close encounters with the sun, IEEE Spectr. 56 (5) (2019) 32–53.
[52] H. Liu, Z. Wei, W. He, J. Zhao, Thermal issues about Li-ion batteries and recent progress in battery thermal management systems: A review, Energy Convers. Manage. 150 (2017) 304–330.
[53] E.G. Colgan, B. Furman, M. Gaynes, W.S. Graham, N.C. LaBianca, J.H. Magerlein, R.J. Polastre, M.B. Rothwell, R. Bezama, R. Choudhary, et al., A practical implementation of silicon microchannel coolers for high power chips, IEEE Trans. Components Packag. Technol. 30 (2) (2007) 218–225.
[54] J. Linn, M.J. Kloker, Effects of wall-temperature conditions on effusion cooling in a supersonic boundary layer, AIAA J. 49 (2) (2011) 299–307.
[55] A.M. Coppola, L.G. Warpinski, S.P. Murray, N.R. Sottos, S.R. White, Survival of actively cooled microvascular polymer matrix composites under sustained thermomechanical loading, Compos. Part A: Appl. Sci. Manuf. 82 (2016) 170–179.
[56] S.J. Pety, M.H.Y. Tan, A.R. Najafi, A.C. Gendusa, P.R. Barnett, P.H. Geubelle, S.R. White, Design of redundant microvascular cooling networks for blockage tolerance, Appl. Therm. Eng. 131 (2018) 965–976.
[57] M.H.Y. Tan, A.R. Najafi, S.J. Pety, S.R. White, P.H. Geubelle, Multi-objective design of microvascular panels for battery cooling applications, Appl. Therm. Eng. 135 (2018) 145–157.
[58] K.B. Nakshatrala, Modeling thermal regulation in thin vascular systems: A mathematical analysis, Commun. Comput. Phys. 33 (4) (2023) 1035–1068.
[59] K.B. Nakshatrala, K. Adhikari, Thermal regulation in thin vascular systems: A sensitivity analysis, Commun. Comput. Phys. 35 (2) (2024) 427–466.
[60] A. Savitzky, M.J. Golay, Smoothing and differentiation of data by simplified least squares procedures., Anal. Chem. 36 (8) (1964) 1627–1639.
[61] P.A. Gorry, General least-squares smoothing and differentiation by the convolution (Savitzky-Golay) method., Anal. Chem. 62 (6) (1990) 570–573.
[62] G. Alemanno, M. D'Amore, A. Maturilli, J. Helbert, G. Arnold, O. Korablev, N. Ignatiev, A. Grigoriev, A. Shakun, A. Trokhimovskiy, Martian atmospheric spectral end-members retrieval from ExoMars thermal infrared (TIRVIM) data., J. Geophys. Res.: Planets 127 (9) (2022) e2022JE00742.
[63] R. Ramesh, R.G. Morgan, D. J., Heat transfer measurements in an expansion tube using infrared thermography, AIAA J. 60 (2) (2022) 883–891.
[64] S. Lee, M. Yovanovich, K. Jafarpur, Effects of geometry and orientation on laminar natural convection from isothermal bodies., J. Thermophys. Heat Transfer 5 (2) (1991) 208–216.
[65] B. Kozanoglu, J. Lopez, Thermal boundary layer and the characteristic length on natural convection over a horizontal plate, Heat Mass Transf. 43 (2007) 333–339.
[66] R. Goldstein, K. Lau, Laminar natural convection from a horizontal plate and the influence of plate-edge extensions., J. Fluid Mech. 129 (1983) 55–75.
[67] S. Samanta, A. Guha, A similarity theory for natural convection from a horizontal plate for prescribed heat flux or wall temperature, Int. J. Heat Mass Transfer 55 (13–14) (2012) 3857–3868.